

Theoretical Study of Radical and Neutral Intermediates of Artemisinin Decomposition

Mírian S. C. Pereira, Rudolf Kiralj, and Márcia M. C. Ferreira*

Laboratório de Quimiometria Teórica e Aplicada, Instituto de Química, Universidade Estadual de Campinas, 13081-970 Campinas, SP, Brazil

Received January 12, 2007

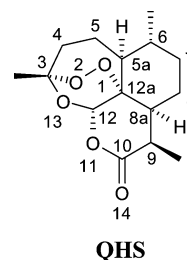
Four artemisinin reductive decomposition routes A, B1, B2, and B3 with 13 species (**QHS**, **1/2**, **3**, **4**, **5**, **5a**, **6**, **7**, **18**, **18a**, **19**, **20**, and **21**) were studied at the B3LYP/6-31G** level. Structures of the species were analyzed in terms of geometrical parameters, Löwdin bond orders, partial atomic charges and spin densities, electronic and free energies, and entropy. Searches in the Cambridge Structural Database for high-level quality artemisinin-related structures were also performed. Principal Component and Hierarchical Cluster analyses were performed on selected electronic and structural variables to rationalize relationships between the routes. The A and B1 routes are possibly interconnected. Structural and electronic features of all species show that there are two clusters: A–B1 and B2–B3. The latter cluster is thermodynamically more favorable ($\Delta\Delta G$ is -64 to -88 kcal mol $^{-1}$) than the former ($\Delta\Delta G$ is -58 to -59 kcal mol $^{-1}$), but kinetical preference may be the opposite. Along the artemisinin decomposition routes, especially B2 and B3, larger structural changes including formation of branched structures and CO $_2$ release are related to increased exothermicity of the conversions, weakened attractive oxygen–oxygen interactions, and increased entropy of the formed species. The intermediate **4** definitely belongs to some minor artemisinin decomposition route.

1. INTRODUCTION

According to the World Health Organization, nowadays malaria is a tropical and parasitic disease that causes more deaths and socioeconomic problems in the world than AIDS. Malaria is one of the diseases that still persist in the world. *Plasmodium falciparum*, responsible for severe malaria, affects the world population by causing 1–1.5 million deaths each year. Malaria occurs mainly in African, Asian, and Latin American countries. The problems of malaria control in these countries are worsened by unsuitable structures in public health area and poor socioeconomic conditions. About 90% of deaths occur in Africa and most of them among children under 5 years of age.¹

Humans can be infected by one of four different species of the parasite: *Plasmodium vivax*, *Plasmodium malariae*, *Plasmodium ovale*, and *Plasmodium falciparum*, the most dangerous species. Malaria is transmitted by inoculation of sporozoites during a bite of an infected female mosquito, *Anopheles*.² The parasite invades and develops within hepatocytes to release merozoites, which quickly invade erythrocytes to grow from “rings” to mature trophozoites, then to schizonts, and finally to release merozoites that invade more erythrocytes, repeating the cycle.³

The malaria parasites are becoming resistant to most antimalarial agents, for example, chloroquine, quinine, and mefloquine.^{4,5} Artemisinin (in Chinese: qinghaosu, **QHS**, Figure 1), originating from *Artemisia annua*, is a potent antimalarial drug against resistant strains of *P. falciparum*. It was isolated for the first time in 1972 by Chinese researchers.⁶ Artemisinin is an endoperoxide containing a sesquiterpene lactone, which has demonstrated to be essential



QHS

Figure 1. The structure and numbering system of artemisinin, qinghaosu (**QHS**).

for antimalarial activity. However, the detailed mechanism of artemisinin action is still not clear,^{7,8} and there are various proposed mechanisms. According to one theory, probably an iron-catalyzed reduction of the endoperoxide bond leads to the formation of oxygen-centered radicals responsible for an oxidative stress⁹ within infected erythrocytes. Other theories^{10–12} propose formation of carbon-centered radicals, alkylants for specific parasites proteins or heme.

In humans, malarial parasites digest more than 70% of hemoglobin within the infected red blood cell,¹³ giving globin and heme as the products. Globin is hydrolyzed into amino acids, which are used in protein synthesis by the parasite. The toxic heme is detoxified by malarial parasite through a specific mechanism of heme polymerization.¹⁴ The polymerized heme, also known as “hemozoin” or “malaria pigment”, accumulates in the form of a crystalline, insoluble, black-brown pigment. A small fraction of the host’s iron is incorporated into a parasite’s metalloproteins such as superoxide dismutase¹⁵ and ferredoxin.¹⁶ Consequently, heme iron or non-heme iron inside the parasite cell is always available for interaction with artemisinin and its derivatives, which can finally result in the parasite’s death.^{12,17}

* Corresponding author phone: +55 19 3521 3102; fax: +55 19 3521 3023; e-mail: marcia@iqm.unicamp.br.

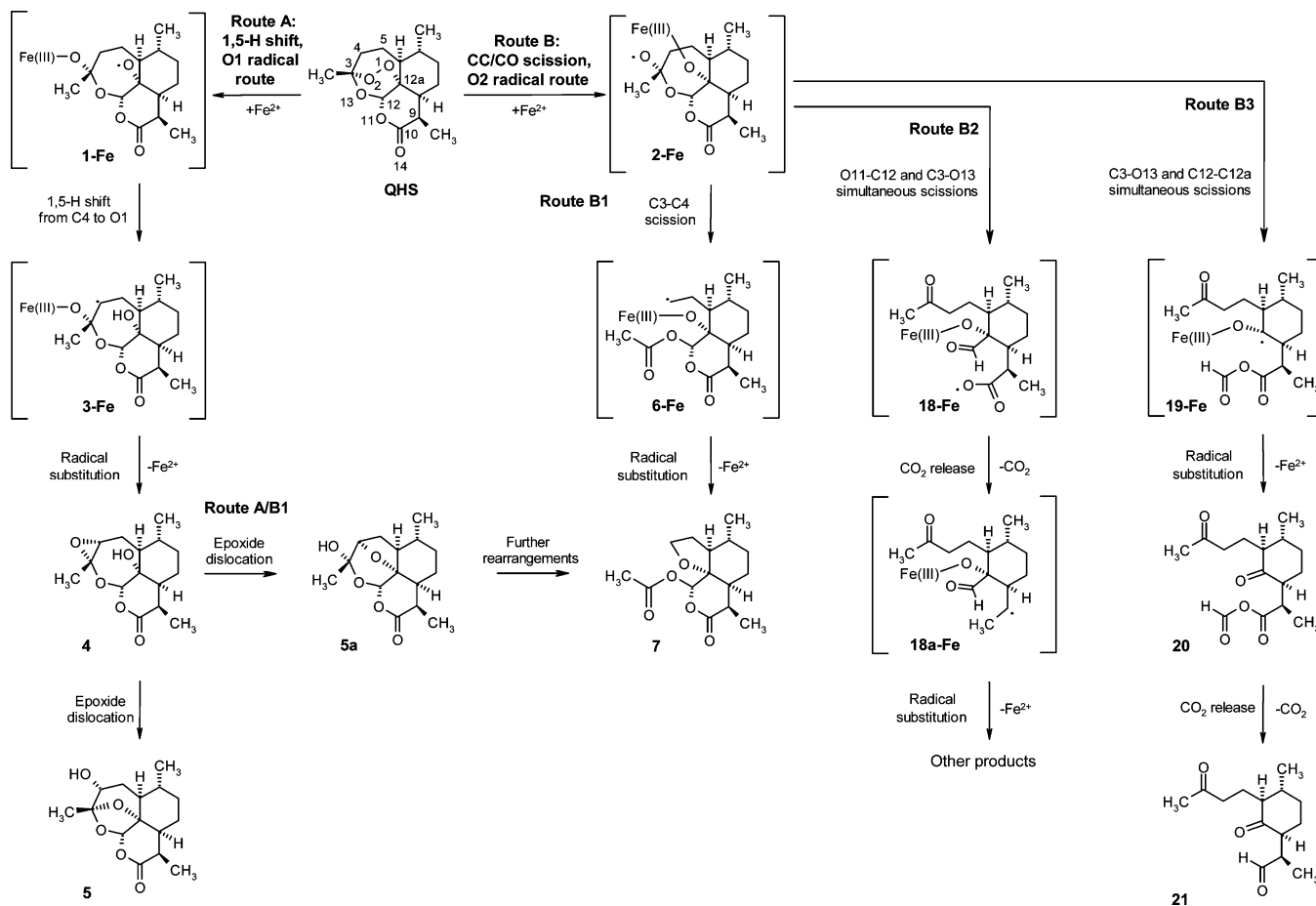


Figure 2. Investigated routes of the iron-catalyzed artemisinin reductive decomposition. Radicals computationally confirmed in this work are in square brackets. All radicals are formally complexed by iron, which is marked by names of the respective complexes. Fe(III) in computational procedures was simulated by an electron, meaning that the radicals were treated as free anions.

The most accepted theory of heme-mediated artemisinin activation is based on the works of Jefford et al.¹⁰ and Meshnick et al.,¹² supported by the experiments of Robert et al.^{17,18} and Posner et al.^{19–21} According to the theory, an oxygen atom from the peroxide gives origin to radical intermediates which interrupt the detoxification process of heme by alkylating heme or hemozoin and, subsequently, disable the parasite activity. Essential intermediates for the alkylation reaction are carbon-centered radicals.

A new theory of artemisinin activation by non-heme iron is based on the work of Eckstein-Ludwig et al.²² and later works,^{7,23} which have proposed that artemisinin does not accumulate in the digestive vacuole and does not inhibit hemoglobin degradation and that artemisinin does not require the presence of heme for its activation. According to this theory, artemisinin is first activated by non-heme iron, and then it binds most probably to the Ca^{2+} -ATPase in the sarco/endoplasmic reticulum of *P. falciparum*. However, it is not known which radicals, oxygen- or carbon-centered, are important for the reaction with Ca^{2+} -ATPase.

Theoretical investigations dealing with the mechanism of trioxanes artemisinin were initiated by Gu et al.,^{24,25} followed soon by several other quantum-chemical works.^{26–33} Molecular modeling and quantitative structure–activity studies on artemisinin^{34–39} have also contributed to the present knowledge about artemisinin behavior. Experimental works on artemisinin decomposition kinetics,^{40–42} reactivity,^{19–21,43–45} photolysis,⁴⁶ thermolysis,⁴⁷ and mass spectrometry⁴⁸ have

provided valuable data and facts about artemisinin decomposition.

In the present work, ab initio B3LYP/6-31G** calculations are performed to investigate a probable mechanism of reductive decomposition of artemisinin. The decomposition routes were selected for the study based on several experimental and theoretical works. Energetic and structural properties of a set of radical anions and neutral species which are formed in these routes are discussed. The computational results can be related to antimalarial, anticancer,⁴⁹ antiangiogenic,^{49,50} and neurotoxicity⁵¹ activities of artemisinin and to its thermal,⁴⁷ electrochemical,⁴³ photochemical,⁴⁶ and spectroscopic^{33,52} properties, pH-dependent reactivity,^{32,45} and ionization behavior.⁴⁸

2. METHODOLOGY

Quantum-mechanical methods implemented in Gaussian 98⁵³ and Titan⁵⁴ programs were used to optimize the artemisinin and intermediates geometries (Figure 2). The artemisinin geometry optimization was carried out by seven different methods: semiempirical AM1 and PM3, ab initio methods at the Hartree–Fock (HF) level with three pseudopotential (CEP - Compact Effective Potentials) basis sets CEP-31G, CEP-31G**, and CEP-31++G** and the basis set 6-31G**, and at the Density Functional Theory (DFT) level with the B3LYP^{55,56} functional and basis set 6-31G**. These calculations were performed in order to find out the

method that would present the best compromise between computational time and accuracy of the results relative to experimental data.

The Cambridge Structural Database (CSD)⁵⁷ January/May 2007 update⁵⁸ via the ConQuest 1.9^{59,60} searching interface was used to retrieve experimental structures of artemisinin and decomposition products from Figure 2. The same software with addition of the Vista⁶¹ statistics interface was applied in finding structural features of the bicyclic ring in artemisinin derivatives, with the following conditions: crystallographic factor $R \leq 5\%$, powder, disordered, and error structures were excluded. The artemisinin structure determined by X-ray crystallography⁶² (CSD: QNGHSU03, $R=5.7\%$) was considered as the most reliable reference structure and so was used as the starting point for all theoretical calculations.

Hierarchical Cluster Analysis (HCA) and Principal Component Analysis (PCA),^{63,64} chemometric methods implemented in Pirouette software,⁶⁵ were used to compare the optimized structures by different methods with the most accurate experimental structures of artemisinin (CSD: QNGHSU03 and QNGHSU10⁶⁶ with $R=3.6\%$) and epiartemisinin⁶⁷ (CSD: WIMMEK, $R=3.5\%$), to identify the appropriate method for further calculations. Both analyses were carried out on an autoscaled data matrix with dimensions 10×18 , where each row was related to 3 experimental and 7 computed geometries, and each column represented one of 18 geometrical parameters of the 1,2,4-trioxane ring: bond lengths and bond and dihedral angles. The ab initio method B3LYP/6-31G** was selected to optimize all structures and used in free energy calculations.

Since the reduction of artemisinin in singlet state (**QHS**) leads to radical anions with an unpaired electron, the unrestricted formalism (UB3LYP) was employed for geometry optimization of these anions. The first radical has an unpaired electron in O1 (**1**, route A), and the second radical has an unpaired electron in O2 (**2**, routes B1, B2, and B3). The radicals **1** and **2** differ only by their formal negative charge and in the location of the unpaired electron. They are supposed to undergo rapid interconversion, and besides, it has been confirmed that they both converge into the same structure at the ab initio level.³² Therefore, only one structure, intermediate **1/2**, was calculated for these species, with the negative charge and the unpaired electron distributed between the two oxygen atoms, according to the literature.^{31,68} Mulliken partial atomic charges were used in this work. The oxidation of the Fe(II) ion into Fe(III) when binding to an oxygen atom from the peroxide bond during formation of the complexes **1-Fe/2-Fe** was simulated in this work by adding an electron to the peroxide group. The literature reports works in which the electron has been simply assigned to the peroxide group in artemisinin^{24,28,31} or in the bicyclic fragment 6,7,8-trioxabicyclo[3,2,2]nonane.^{25,26} There are also works in which a hydrogen atom has been used to simulate the presence of iron or acid interacting with the peroxide group in artemisinin or in the bicyclic fragment.^{29,31,32} Drew et al.³⁰ were the only ones that studied computationally the interactions of artemisinin and the bicyclic fragment with heme iron and hydrated iron. The present work brings a more systematic study of artemisinin decomposition that should precede a study with iron complexes, thus iron was not included in the computations.

Oxygen–oxygen nonbonding distances are rather short in artemisinin³⁵ and can be considered as secondary bonds⁶⁹ via through-bond and through-space interactions involving oxygen lone pairs.⁷⁰ Such distances appear also in species from Figure 2. Geometry optimizations of artemisinin in the triplet state (**QHST**), artemisinin biradical dianion in the triplet state (**QHS²⁻**), radical cation in the doublet state (**QHS⁺**), and biradical dication in the triplet state (**QHS²⁺**) were performed in the same way as for the singlet artemisinin **QHS**, in order to rationalize the relationship between atomic charges, reactivity, and bond length of the peroxide group. Löwdin bond orders⁷¹ were calculated for optimized geometry of all studied species by using Titan. The importance of O–O interactions in artemisinin decomposition and recognition of related electronic structure patterns were inspected by applying PCA and HCA on selected electronic and structural descriptors.

3. RESULTS AND DISCUSSION

3.1. Selection of the Computational Method. Optimized geometry of the 1,2,4-trioxane fragment in **QHS** from semiempirical and ab initio methods is compared with the experimental results in Table 1. In general, a good agreement exists between the experimental and calculated parameters. It is obvious from Table 1, that the calculated peroxide and the C–O bond distances from HF ab initio methods are too short compared to the experimental values. Short bond lengths have also been reported in earlier studies of artemisinin,^{72,73} leading to the conclusion that the HF method overestimates the bonding ability of the oxygen atom. The B3LYP method reproduces very well these distances, with the differences between calculated and experimental values within experimental errors (Table 1).

Hierarchical Cluster Analysis and Principal Component Analysis were the chemometric methods used with the objective to identify which geometry optimization method is the closest to the experimental results. The advantage in using such methods is that all structural parameters are considered simultaneously, and correlations among them are taken into account. Analyzing the dendrogram obtained by HCA with incremental linkage method in Figure 3, left, it can be concluded that the geometrical parameters calculated by the DFT-B3LYP method gave the best results once they form a single cluster with the experimental parameters (similarity index is 0.60). Besides that, it can be observed that the methods with polarization functions, HF/6-31G**, HF/CEP-31G**, and HF/CEP-31++G**, form another cluster with a very small similarity index with the experimental methods (0.28), while the semiempirical methods and HF/CEP31G form the third cluster that has nothing in common with the experimental data.

PCA was used also to investigate the most appropriate method for further calculations. The PC1–PC2 scores plot, describing 65% of the original information, is shown in Figure 3, right. The computational methods are distributed in a similar way as in HCA: ab initio methods are on the left side and the semiempirical methods are on the right side. B3LYP with polarization functions provided the closest results to the experiments, while the HF methods are more distant and form a cluster.

Geometry optimization and all subsequent calculations were carried out at the B3LYP/6-31G** level. The doublet

Table 1. Experimental and Calculated 1,2,4-Trioxane Geometries in Artemisinin at Semiempirical and Ab Initio Levels and the DFT Geometry of 1/2

geometry ^a	EXP-Q1 ^b	EXP-Q2 ^c	EXP-EA ^d	PM3	AM1	HF/ CEP-31G	HF/ CEP31G**	HF/ CEP31++G**	HF/ 6-31G**	B3LYP/ 6-31G**	B3LYP/ 6-31G** (1/2) ^e
O1–O2	1.469(2)	1.474(4)	1.481(4)	1.544	1.289	1.439	1.395	1.395	1.390	1.460	2.186
O2–C3	1.416(3)	1.418(4)	1.411(6)	1.403	1.447	1.447	1.405	1.405	1.396	1.414	1.325
C3–O13	1.445(3)	1.451(4)	1.452(6)	1.428	1.427	1.449	1.418	1.417	1.409	1.442	1.521
O13–C12	1.380(3)	1.388(4)	1.396(6)	1.403	1.416	1.413	1.384	1.384	1.376	1.396	1.369
C12–C12a	1.523(2)	1.528(5)	1.514(7)	1.555	1.537	1.549	1.542	1.541	1.532	1.539	1.555
C12a–O1	1.462(3)	1.450(4)	1.466(5)	1.426	1.468	1.479	1.438	1.438	1.430	1.456	1.370
O1–O2–C3	108.1(2)	107.7(2)	109.0(3)	110.3	112.5	109.4	109.5	109.4	109.5	108.3	94.9
O2–C3–O13	106.6(2)	107.1(2)	107.1(3)	104.8	103.6	106.8	108.0	107.9	107.8	108.5	112.6
C3–O13–C12	114.2(2)	113.6(3)	113.6(4)	116.0	115.5	116.8	114.8	115.0	115.3	114.1	117.0
O13–C12–C12a	114.5(2)	114.7(2)	113.3(4)	115.2	113.5	112.5	112.5	112.5	112.3	113.3	116.5
C12–C12a–O1	110.7(2)	111.1(2)	109.7(4)	113.2	111.1	110.6	110.5	110.7	110.6	111.4	114.1
C12a–O1–O2	111.1(1)	111.6(2)	110.9(3)	112.3	113.7	113.4	112.5	112.5	112.7	111.6	107.6
O1–O2–C3–O13	−75.5(2)	−75.5(3)	−73.5(4)	−73.3	−77.8	−72.0	−73.8	−73.9	−73.4	−74.0	−68.8
O2–C3–O13–C12	36.0(2)	36.3(4)	32.8(5)	52.8	42.1	32.9	31.1	31.3	31.1	32.9	44.9
C3–O13–C12–C12a	25.3(2)	24.8(4)	30.3(6)	2.7	11.4	25.5	27.4	27.1	27.4	27.4	31.7
O13–C12–C12a–O1	−51.3(2)	−50.8(4)	−56.8(5)	−40.5	−41.8	−49.7	−50.3	−49.8	−50.1	−51.2	−58.4
C12–C12a–O1–O2	12.6(2)	12.3(3)	17.0(5)	20.0	12.1	12.7	10.8	10.4	10.9	11.6	19.9
C12a–O1–O2–C3	47.8(2)	47.7(3)	45.2(4)	35.6	47.1	46.6	48.9	49.1	48.7	48.0	39.3

^a Bond lengths are in Å, and bond and dihedral angles are in degrees. ^b Experimental structure of **QHS** determined by X-ray crystallography (CSD: QNGHSU03). ^c Experimental structure of **QHS** determined by X-ray crystallography (CSD: QNGHSU10). ^d Experimental structure of epiartemisinin determined by X-ray crystallography (CSD: WIMMEK). ^e Geometry of the radical anion 1/2 as obtained at the B3LYP/6-31G** level.

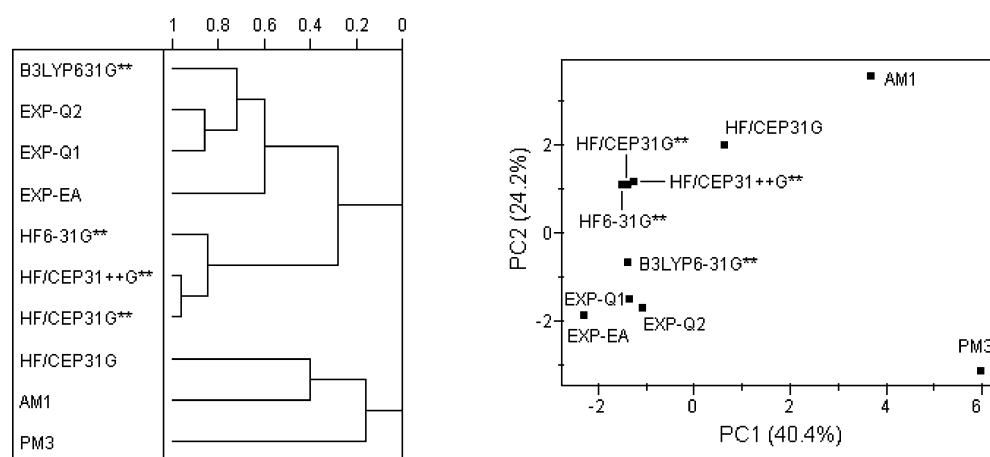


Figure 3. Left: Dendrogram obtained from experimental and optimized structural parameters of **QHS**. Right: PC1–PC2 scores plot of three experimental and seven theoretical results used in the geometry optimization of **QHS**. Experimental structures: EXP-Q1, EXP-Q2, and EXP-EA stand for crystal structures with the CSD codes QNGHSU03, QNGHSU10, and WIMMEK, respectively.

nature of the radicals was confirmed by the expectation value of the operator S^2 , which is exactly 0.75 for a true state. All radicals from Figure 2 showed S^2 values between 0.7534 and 0.7564, clearly characterizing the doublet state.

3.2. Structural Description of the Artemisinin Decomposition. **3.2.1. Artemisinin and Radical Anion 1/2.** According to experimental studies by Posner et al.¹⁹ and by Jefford et al.,¹⁰ the reaction between artemisinin and heme Fe(II) starts with an electron transfer from the cation to the peroxide bond. This results in two possible oxygen centered radical anions **1** and **2** and corresponding complexes **1-Fe** and **2-Fe** (Figure 2), where each one follows a different route with different final products. Optimized geometries of the ground states of artemisinin **QHS** (singlet) and radical anion 1/2 (doublet) are in Figure 4. The geometries of the respective 1,2,4-trioxane fragments are compared in Table 1. Spin density and atomic charge distributions of **QHS** and 1/2 are compared with those of other radicals in Tables 2 and 3. Löwdin bond orders for oxygen–oxygen interactions were

calculated for all studied species because they are logarithmically related to the corresponding distances and are highly correlated with valence bond orders, as is illustrated in Figure A and Tables A and B in the Supporting Information.

According to some spectroscopic^{33,52} and ab initio studies,^{33,51,52} **QHS** possesses two reactive groups—the endoperoxide O1–O2 and carbonyl C10=O14 from which the former is more reactive, responsible for chemical behavior and biological activities (antimalarial, neurotoxicity, anti-cancer) of this compound and its derivatives. The studies show also that all five oxygen atoms interact via through-bond and through-space interactions³³ forming a continuous region of negative electrostatic potential.⁵¹ These interactions and peroxide-hydrocarbon moiety interactions result in certain nucleophilicity or electron donating ability of the O1–O2 group which, when increases by substitutions, destabilizes the peroxide group and makes it more reactive with respect to Fe(III) ion.⁵² The 1,2,4-trioxane ring and the seven-

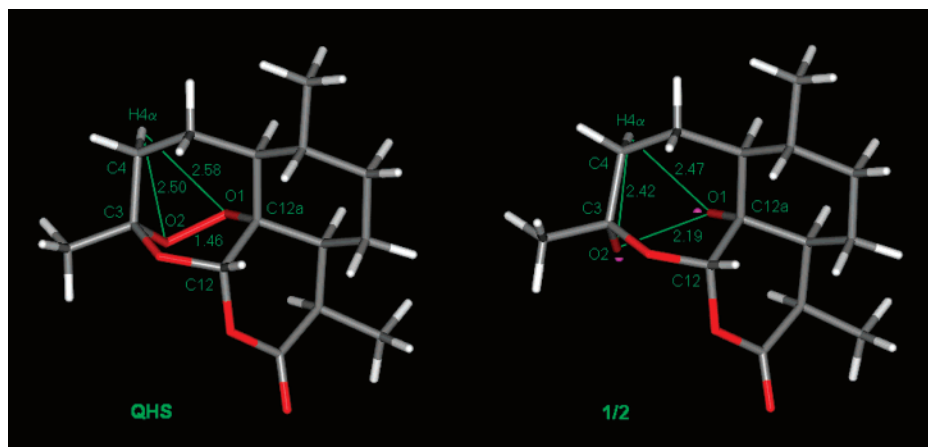


Figure 4. Artemisinin (**QHS**) and intermediate **1/2** bond lengths and interatomic distances in Å. Pink ball halves show the radical delocalization between O1 and O2.

Table 2. Spin Densities^a on Selected Atoms of the Radical Anions

atom	1/2	3	6	18	18a	19
O1	0.4473	0.0125	0.0331	0.3880	0.0321	0.1624
O2	0.5099	0.0373	5×10^{-5}	0.0003	0.0001	0.0017
O11	0.0009	-0.0002	-4×10^{-5}	0.1849		-0.0051
O13	0.0076	0.0089	9×10^{-6}	0.0101	0.0067	0.0418
O14	0.0004	0.0002	0.0002	0.0792		0.0095
C4	0.0123	0.9999	1.0262	0.0007	-0.0002	0.0020
C9	-0.0016	0.0004	-0.0009	0.1308	0.9612	0.0005
C10	0.0001	0.0001	2×10^{-5}	0.0206	-0.0726	0.0263
C12a	-0.0220	-0.0047	-0.0039	0.0067	0.0588	0.6108

^a Values related to principal spin density sites are boldface.

Table 3. Mulliken Partial Atomic Charges of Selected Atoms in Radical Anions^a

atom	1/2	3	6	18	18a	19
O1	-0.518	-0.759	-0.751	-0.544	-0.681	-0.510
O2	-0.541	-0.804	-0.499	-0.537	-0.572	-0.535
O11	-0.484	-0.437	-0.499	-0.588		-0.477
O13	-0.604	-0.566	-0.436	-0.489	-0.522	-0.552
O14	-0.560	-0.553	-0.511	-0.601		-0.542
C4	-0.276	-0.470	-0.246	-0.155	-0.155	-0.057
C9	-0.050	0.049	-0.152	0.004	-0.231	-0.027
C10	0.640	0.612	0.599	-0.682	-0.337	0.702
C12a	0.129	0.229	0.339	0.282	0.433	-0.207

^a Charge values related to principal spin density sites from Table 2 are boldface.

membered ring are in a twist-boat conformation in the crystalline state.^{62,67} Besides, according to vibrational analyses,^{33,72,73} the peroxide bond is rather strongly coupled with the surrounding carbon skeleton. A systematic search in the CSD resulted in 18 high-quality crystal structures of artemisinin and its derivatives, which contain 27 structural samples of an artemisinin skeleton (Table C and Figure B in the Supporting Information). In these samples, the O1–O2 bond length exhibits observable variation in the range of 1.448–1.482 Å and with the mean value 1.472 Å which is equal to the peroxide bond length in hydrogen peroxide (1.475 Å).⁷⁴ The peroxide bond length variations are mainly due to intramolecular interactions and less to crystal packing forces, but the bond length shows a systematic decrease with the increase of the bond angle O2–O1–C12a which varies from 110.9 to 113.2° (correlation coefficient $r = -0.554$). The torsion angle C3–O2–O1–C12a varies from 40.0 to 49.8° in the crystal structure samples and is rather well

negatively correlated with the angle C3–O2–O1 which varies from 107.3 to 109.9° ($r = -0.735$). These two correlations show a rather modest partial double character of the O1–O2 bond and sp^2 hybridization of the oxygen atoms, confirming the electron-donating and not electron-withdrawal nature of the peroxide environment.⁷⁵ The O1–O2 bond in **QHS** structure from Figure 4 has a Löwdin bond order of 1.13.

The reactive O1–O2 bond undergoes homolytic scission during pyrolysis,⁴⁷ ionization,⁴⁸ and photolysis,⁴⁶ resulting in the triplet biradical **QHST**.⁷⁶ DFT calculations in this work show that **QHST** has a rather large separation of O1 and O2 (2.614 Å) which is between weak secondary bonds and van der Waals contacts, while the spin density is almost equal at O1 and O2 (0.80 and 0.85, respectively). However, the first and second ionization lead to similar partially double O1–O2 bonds in **QHS**⁺ and **QHS**²⁺ (1.342 and 1.330 Å, respectively). Unusually small Mulliken charges (from -0.05 to -0.10) and noticeable spin densities (0.4–0.5) are located at O1 and O2 in both species, while high spin density is on carbonyl O5 (0.71) and high positive charge at C10 (0.72) in **QHS**²⁺. Such radical characterization is in agreement with the literature about the reactivity nature of artemisinin.^{33,52} However, the first and second one-electron reductions of **QHS** produce radical anions **1/2** and **QHS**²⁻, respectively, in which the scission of the O1–O2 bond does not result in the large separation of the oxygen atoms like in **QHST** but in similar secondary bonds in these species. Pronounced spin densities at O1 and O2 in **1/2** (Table 2) and **QHS**²⁻ (O1: 0.52, O2: 0.42) and similar Mulliken charges (from -0.52 to -0.55) in both species show the first electron absorption by the peroxide bond. The second absorption by the carbonyl group is visible in **QHS**²⁻ from the spin density on C10 (0.57), Mulliken charge at O14 (-0.68), and the loss of the planarity of this group. The radical anion **1/2** is the key intermediate in the artemisinin one-electron reductive scheme in this work (Figure 2). The secondary bond length O1–O2 is 2.186 Å, which corresponds to Löwdin bond order 0.23, meaning that there is a certain resonance of the absorbed electron between O1 and O2. The same O1–O2 distance (2.185 Å) has been obtained by Taranto et al.³¹ at the B3LYP/6-31G* level. The literature⁷⁷ reports short nonbonding distances between oxygen anions in inorganic oxides, with the minimum value of 2.054 Å, which indicates attractive



Figure 5. Interatomic distances involving the H4 α and the radical carbon atom C4 (in Å) and bond angles (deg) around C4 of intermediates **3** and **6**. The strong hydrogen bond in **3** and the C–H... π interaction in **6** are well visible. Pink balls show the radical localization at C4.

rather than repulsive oxygen–oxygen interactions. Comparing the trioxane geometries in **QHS** and **1/2**, one can notice significant structural changes in the neighborhood of O1 and O2 (Table 1), especially the shortening of the O1–C12a and O2–C3 bonds due to their partial double bond character after electron absorption. These bond are, however, still much longer than pure double C=O bonds (like carbonyl C10=O14 in **QHS**: 1.207 Å, and in **1/2**: 1.220 Å), which reconfirms that C3–O2–O1–C12a is a one-electron delocalized system. The twist-boat conformations of the trioxane and seven-membered rings and rigid conjunctions of the rings at the quaternary C3 and C12a can be steric reasons that prevent the large separation of O1 and O2.

High-level DFT calculations of Drew et al.³⁰ have shown that O1–O2 separation is 2.442 Å and nonbonding Fe(II)–O2 distance is 3.568 Å when O1 from **QHS** is coordinated to iron in [Fe(H₂O)₆]²⁺. The oxygen atoms still remain in a secondary bond, while O2 makes the second coordination sphere of Fe^{27,35,38,39} and, thus, weakly interacts with the metal (the maximum van der Waals contact for iron and oxygen is 3.86 Å, as verified by the program Platon⁷⁸). The electronic structure of **1/2** indicates almost equal chances for formation of **1** and **2** complexed with iron due to coupled electronic and steric effects involving the peroxide group,⁷⁹ and therefore, very similar probabilities for artemisinin decomposition to follow routes A and B1 (Figure 2). Several experimental evidences^{10,41,43–45,47,48} for artemisinin decomposition show that the final products composition of artemisinin degradation can vary from high preference for route A to prevalence of route B, depending on the experimental conditions: type of decomposition (photolysis/thermolysis, ionization, electrochemical, or some chemical), catalyzer (transitional metal and its chemical form), solvent, pH, anions and other present species, and treatment of the reaction mixture. This fact justifies the described computational treatments of **1/2** in the present study.

3.2.3. Route A. The most recent theoretical study of artemisinin reductive decomposition which deals with artemisinin skeleton is the work of Taranto et al.³¹ The authors studied route A from **1/2** to **5** and route B from **1/2** to **7** (B1), **18** (B2), and **20** (B3). The structural, electronic, and thermodynamic results of their mechanistic studies are consistent with the results of the present work. Besides that, the present work brings three extensions of this scheme

(Figure 2). In one, the alternative route A/B connects A and B1 via **5a**,^{44,47} a relatively unstable intermediate that has been rarely considered in artemisinin degradation. **5a** could be formed from **4** simultaneously with **5** and later rearranged into **7**. This A/B mechanism may contribute, besides the structural features of **1/2**, to similar product yields of routes A and B1.^{10,47} Two other extensions are CO₂ releasing steps, a catalyzed radical decomposition **18** → **18a**,⁴⁴ and a noncatalyzed product degradation **20** → **21**.^{10,45}

Route A is the so-called 1,5-H shift or the O1 radical route (Figure 2), because it starts with the 1,5-hydrogen transfer in 1,2,4-trioxanes⁸⁰ during which the iron-mediated formation of radical anion **1** (Figure 4) continues with the rearrangement of **1** into alcohol **3** with OH at O1 (Figure 5, left). Steric (more hydrogen atoms) and electronic features (proximity to the peroxide group) of C4 and C5a favor the former carbon for the hydrogen transfer and formation of the secondary carbon-centered radical **3**, which is visible from the location of the unpaired electron at C4 (Table 2) which is sp²-hybridized (the bond angles sum is 358°, Figure 5, left). Hydrogen bonding interactions are the driving forces for this transfer, because the H4 α hydrogen at C4 is only 2.4–2.5 Å away from the peroxide group in **1/2** (Figure 4, right) and 2.5–2.6 Å in **QHS** (Figure 4, left), and the corresponding Löwdin bond orders are 0.010–0.013 and 0.005–0.006, respectively. These bond orders are among the highest values for all C/O...H interactions in **QHS** and **1/2**. Besides, there are 22 artemisinin fragments in 16 structures from the CSD (Table C), showing relatively small variability of these distances (2.38–2.65 Å, with the mean of 2.51 Å). **3** is stabilized by a strong hydrogen bond between O1 and O2 (Figure 5, left). Fe(II) removal may cause formation of the epoxide **4** (Figure 6, left) which decomposes into alcohols **5** and **5a** (Figure 6, right). **4** was proposed by Posner et al.^{19,21} as responsible for the parasiticidal activity of artemisinin due to its potent alkylating property. However, Avery et al.⁸¹ performed a set of experiments trying to stabilize **4**, but there was no evidence for its formation. The DFT and experimental (CSD: DIJDEF⁴⁷) geometries of **5** are well overlapped, with small differences at the hydrogen-bonding groups (hydroxyl and carbonyl) due to their involvement in hydrogen bonds in the crystalline state. The OH group in **5a** forms a weak hydrogen bond with O2, which is not sufficient to prevent interconversion **5a** → **7**.

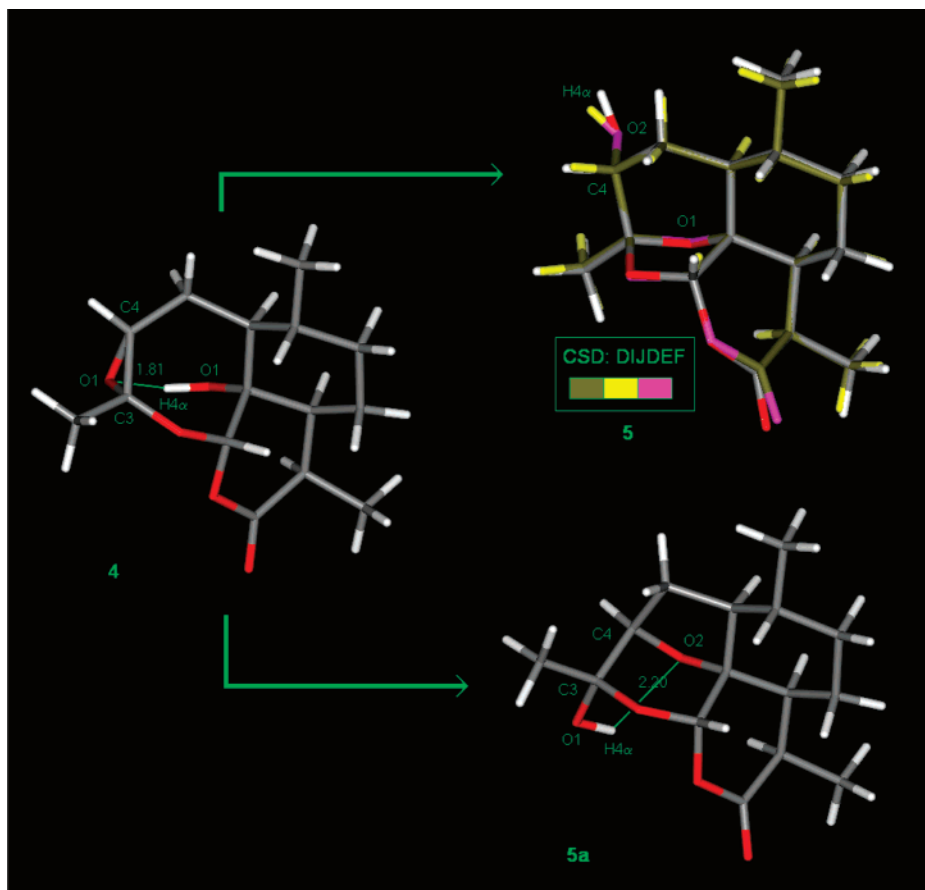


Figure 6. Conversion of the intermediate epoxide **4** into **5** and **5a**. The strong hydrogen bond in **4** and the weak one in **5a** are visible. The intermediate **5** is shown as the overlap of B3LYP and experimental (CSD: DIJDEF, colored differently) geometries.

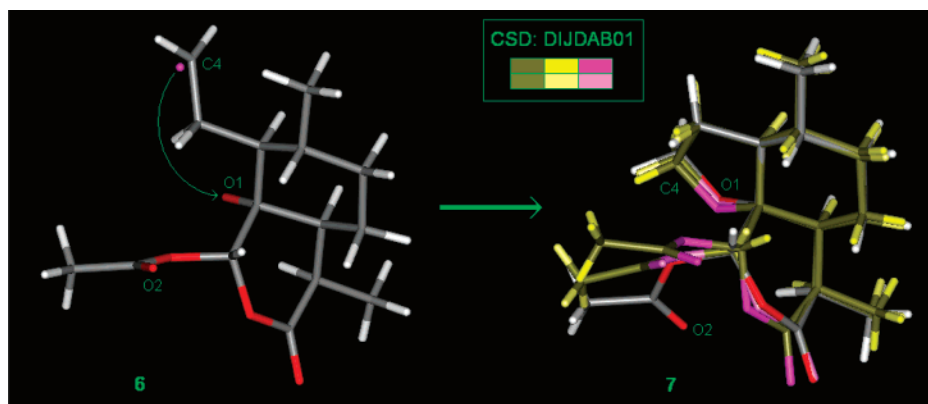


Figure 7. Route B1: Oxidation of the radical **6** (pink ball showing the radical localization) into the intermediate **7**. **7** is shown as the overlap of B3LYP and two experimental (CSD: DIJDAB01, colored differently) geometries.

3.2.2. *Routes B.* The three B routes (Figure 2) begin with the O2-centered radical **2** and continue with one (carbon–carbon) or two (carbon–oxygen and carbon–carbon) bond scissions. The primary carbon-centered radical **6** (Figure 5, right) is formed by opening the seven-membered ring. Spin densities (Table 2) show the location of the unpaired electron at C4, which is sp^2 -hybridized (the bond angles sum is 359° , Figure 5, right) and behaves as a π donor by forming a C–H... π interaction with a hydrogen atom from the methyl group at C6. Route B1 ends in **6** \rightarrow **7** oxidation, in which Fe(II) is removed from **6-Fe** and O2 and C4 close a tetrahydrofuran ring (Figure 7). The DFT and two experimental (CSD: DIJDAB01⁸²) geometries of **7** are reasonably well overlapped, with differences at the carbonyl group and

a flexible side chain at C12 due to their involvement in C–H...O interactions in the crystalline state.

Taranto et al.³¹ and previous researchers have not confirmed computationally the existence of a putative radical, proposed in earlier literature, which would be formed from **2** by the C3–O13 scission and then could decompose into **18** via the O11–C12 scission or into **19** via the C12–C12a scission. The same happened in this work, when the initial geometry of this intermediate radical converged into the geometry of **19**. Besides, the initial geometry of another test radical, modeled from **2** by O11–C12 scission, converged into the geometry of **18**. These results indicate that putative intermediates for **2** \rightarrow **18** and **2** \rightarrow **19** conversions do not exist and that **18** and **19** are formed from **2** by synchronized

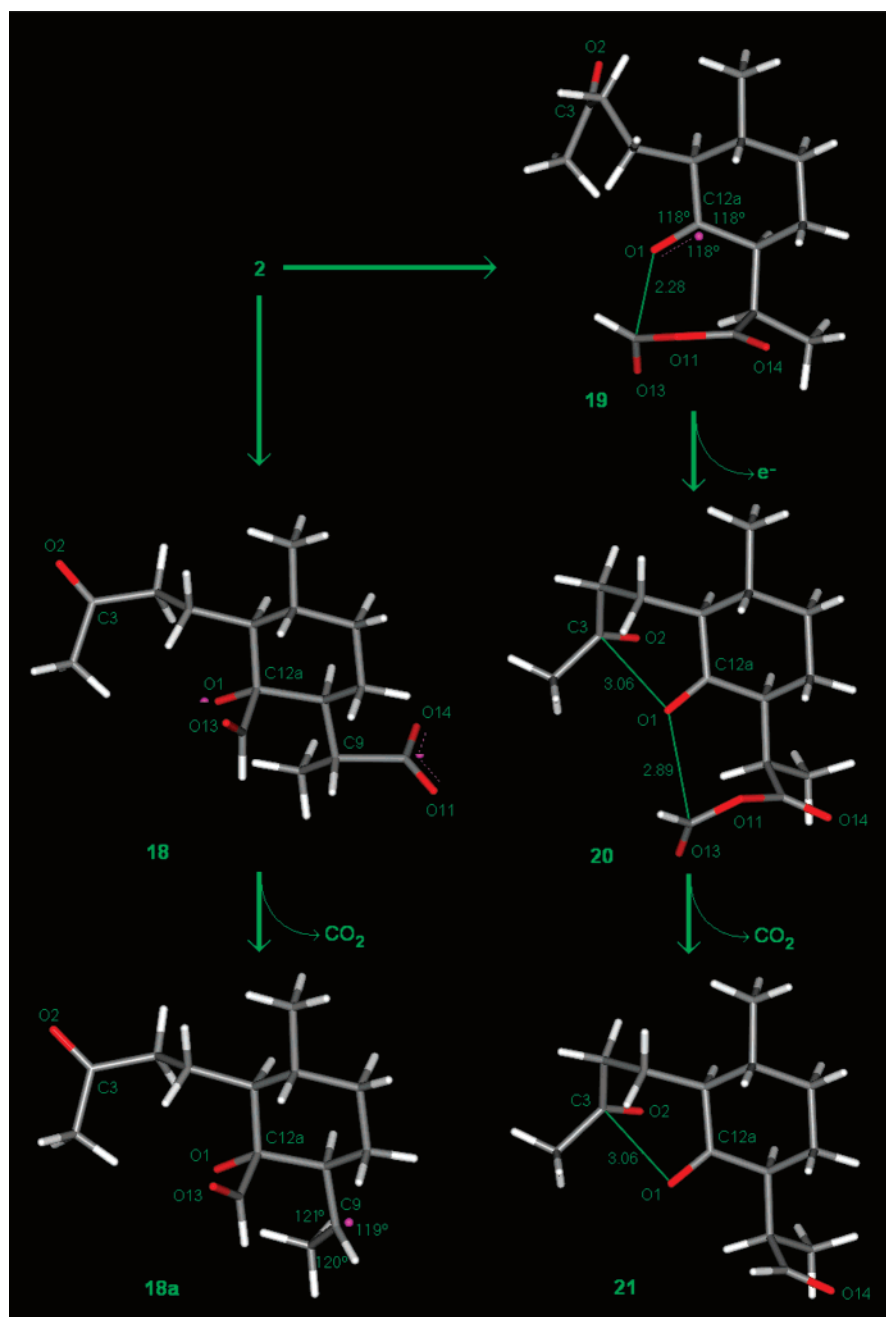


Figure 8. Reaction routes B2 (left) and B3 (right). Interatomic distances (in Å) involving O1 and bond angles (deg) around radical atoms C9 and C12a are shown for **18a** and **19–21**. Pink balls, ball halves, and dashed lines show radical localization or partial delocalization.

scissions of two chemical bonds because eventual disruption of only one bond would generate very unstable species. A chemical explanation for the formation of **18** from **2** is due to the fact that the seven-membered ring opens by homolytic disruption of the weaker carbon–oxygen bond (the bond C3–O13 is longer than C12–O13, Table 1). During the scission of this bond, a stable oxygen triad O13–O11–O14 is formed via through-bond and through-space interactions,⁷⁰ probably including partial delocalization of the radical electron. This triad may act on the C12–C12a bond as an electron-withdrawing fragment via inductive and resonance effects, which causes the homolytic scission of this bond. Formation of **19** from **2** can be explained in a similar way. The carbonyl-containing six-membered ring opens by homolytic disruption of the weaker carbon–oxygen bond (O11–C12 is longer than C10–O11 due to the conjugation

effect of C10=O14 on C10–O11). During this bond scission, two new formal radical centers are formed, at C12 and O11. While the O11 center is stabilized by delocalization within the carboxyl group, the C10 and O2 radicals disappear in a new rearrangement which requires homolytic scission of the C3–O13 bond.

18 is formally a radical anion coordinated to Fe(III) in **18-Fe**, confirmed experimentally by Wu et al.⁴⁴ and theoretically by Denisov et al.⁴⁰ The physical absence of iron during the computational procedure in this work has resulted in a species with the unpaired electron delocalized between O1 and the carboxyl radical with C9 (Figure 8), as visible from spin densities (Table 2) and atomic charges (Table 3). This electron delocalization was also reported by Taranto et al.^{31,68} Bond lengths show that the carbonyl bonds are essentially double (C3=O2: 1.221 Å, C12=O13: 1.218 Å, and the

Table 4. Electronic Energy, Gibbs Free Energy, and Total Entropy of Artemisinin and Its Decomposition Intermediates

structures ^a	E_e/au^b	$\Delta G/\text{au}^b$	$S_{\text{tot}}/\text{cal mol}^{-1} \text{K}^{-1}$
QHS	-960.920335	-960.602290	128.8
1/2	-960.973456	-960.661659	132.9
3	-960.984747	-960.677166	134.8
4	-960.960467	-960.643256	131.8
5	-961.012164	-960.694837	131.8
5a	-961.004769	-960.685930	129.7
6	-960.974604	-960.675138	151.9
7	-961.009897	-960.696148	138.4
18	-960.994860	-960.698265	158.7
18a+CO₂	-960.981892	-960.703610	188.0
19	-961.009149	-960.708315	151.3
20	-961.013869	-960.711300	156.8
21+CO₂	-961.025427	-960.742927	193.5

^a The sum of the energies of two products is presented: **18a** and **CO₂** and **21** and **CO₂**. ^b Atomic unites (hartrees).

Löwdin bond orders are 2.19 and 2.20, respectively), and the O1–C12a is partially double (1.341 Å, the bond order is 1.41). The carboxyl C–O bonds are almost indistinguishable, with extremely high double bond character (the lengths around 1.24 Å and bond orders 1.91–1.98). However, C9–C10 is a weakened bond 1.686 Å long and with a bond order of 1.07. This can explain why the scission of this bond results in **CO₂** and a new radical anion **18a** which is still coordinated to Fe(III) in **18a-Fe** but with the unpaired electron localized at C9 (Table 2). Further decomposition may continue from **18a**.

Route B3 starts with the C12a-centered anion radical **19**, which is stabilized by the unpaired electron delocalization along the O1–C12a bond (Table 2) and a secondary bond between the electrophilic O1 radical and the nucleophilic C12=O13 bond (the Löwdin bond order for O1...C9 is 0.20). C12a is sp²-hybridized, since the bond angles sum is 356° (Figure 8, right). This interaction is weakened when Fe(II) is removed from **19-Fe**, but another similar one is established between O1 and C3, by which the three side chains are mutually stacked in the product **20**. The next step, the **CO₂** release, does not affect overall skeletal conformation and the strength of the O1...C3 interaction (Figure 8, right). **20** can undergo further decomposition, which would be interesting to study in the future.

3.3. Electronic Energy Description of the Artemisinin Decomposition. **3.3.1. Comparison of Routes A and B1.** Electronic energies of all species studied at the B3LYP/6-31G** level are in Table 4. Electronic energy differences related to one or more steps in the artemisinin decomposition routes are in Table 5, and the final energy summary for the routes is presented in Table 6. The energy release of 33.33 kcal mol⁻¹ was obtained for the formation of **1/2** from **QHS**, which corresponds to the energy of homolytic scission of a relatively weak covalent bond, the peroxide bond. This value is close to the experimental value for artemisinin (30.7 kcal mol⁻¹),⁸³ also being close to values for various 1,2,4-trioxanes (about 30 kcal mol⁻¹)⁸⁴ and acyclic organic peroxides (about 36.3 kcal mol⁻¹).⁸⁵ The literature on organic peroxide reports steric effects as destabilizers of the peroxide bond.⁸⁵ Hyperconjugation effects of the neighboring C–C bonds to the oxygen atoms are stabilizers of alkyl radicals,⁸⁶ which may explain the earlier observations in this work, according to which **1/2** is a “resonant hybrid of **1** and **2**”.³¹

Table 5. Electronic Energy Difference (ΔE_e), Total Gibbs Free Energy Difference ($\Delta\Delta G$), and Entropy Difference (ΔS) Important for Artemisinin Decomposition Routes

difference	$\Delta E_e/\text{kcal mol}^{-1}$	$\Delta\Delta G/\text{kcal mol}^{-1}$	$\Delta S/\text{cal mol}^{-1} \text{K}^{-1}$
QHS – 1/2	-33.33	-37.25	4.1
1 – 3	-7.09	-9.73	1.9
3 – 4	15.24	21.28	-2.9
4 – 5	-32.44	-32.37	0.0
1 – 5	-24.29	-20.82	-1.1
4 – 5a	-27.80	-26.78	-2.1
5a – 7	-3.22	-6.41	8.6
2 – 6	-0.72	-8.46	19.0
6 – 7	-22.15	-13.18	-13.5
2 – 7	-22.87	-21.64	5.5
2 – 18	-13.43	-22.97	25.8
18 – 18a+CO₂	8.14	-3.35	29.3
2 – 18a+CO₂	-5.29	-26.32	55.1
2 – 19	-22.40	-29.28	18.4
19 – 20	-2.96	-1.87	5.5
20 – 21+CO₂	-7.25	-19.85	36.7
2 – 20	-25.36	-31.15	23.9
2 – 21+CO₂	-32.61	-51.00	60.6

Table 6. Total Electronic Energy Difference (ΔE_e), Total Gibbs Free Energy Difference ($\Delta\Delta G$), and Entropy Difference (ΔS) of Each Route in Artemisinin Reductive Decomposition

routes ^a	$\Delta E_e/\text{kcal mol}^{-1}$	$\Delta\Delta G/\text{kcal mol}^{-1}$	$\Delta S/\text{cal mol}^{-1} \text{K}^{-1}$
route A → 5	-57.62	-58.07	3.1
route A → 5a	-52.98	-52.48	1.0
routes A/B1 or B1 → 7	-56.20	-58.89	9.6
route B2 → 18	-46.76	-60.22	29.9
route B2 → 18a+CO₂	-38.62	-63.57	59.2
route B3 → 20	-58.69	-68.40	28.0
route B3 → 21+CO₂	-65.94	-88.25	64.7

^a A/B1 denotes two routes with the same final product **7**. Route A can result in **7** via **5a** rearrangement, while route B1 results only in **7**.

Tables 4–6 contain electronic energy results for all routes of artemisinin decomposition. Conversion of the O2-centered radical **1** into the secondary C-centered radical **3** via 1,5-hydrogen shift is exothermic, partially due to C/O–H...O hydrogen bond rearrangements (Figures 4 and 5). However, the oxidation of **3** into **4** with epoxide ring formation is rather endothermic. It is clearly observed that the conversion **4** → **5** is favorable (Table 5). Another possibility for the epoxide opening can result in **5a** which has OH at C3, although this process is less favorable than **4** → **5** by 4.6 kcal mol⁻¹. The new species is still instable and converts into **5** with a small energy release (3.2 kcal mol⁻¹). Finally, **1** → **5** is more exothermic than **1** → **7** only by 1.4 kcal mol⁻¹.

Route B1, unlike route A, starts with slightly exothermic conversion of the O1-centered radical **2** into the primary C-centered radical **6** via the seven-membered ring opening. The next step in which **6** is oxidized, the tetrahydrofuran formation, results in significant energy release (–22.2 kcal mol⁻¹). **3** is more stable than **6** by 6.4 kcal mol⁻¹, indicating that the 1,5-hydrogen atom shift, compared to this C–C bond scission route, could have some preference. Recent thermodynamic studies^{24,25} have shown that the activation energy and compound energy formation for the 1,5-hydrogen atom shift in intermediate **1** are lower than those of the C–C bond cleavage process. From the chemical point of view that would be feasible since the 1,5-hydrogen atom shift includes rearrangement of more reactive groups, while for formation of **6** more bond cleavages are required, and, so, the rate of formation of radical **6** would be less preferable.

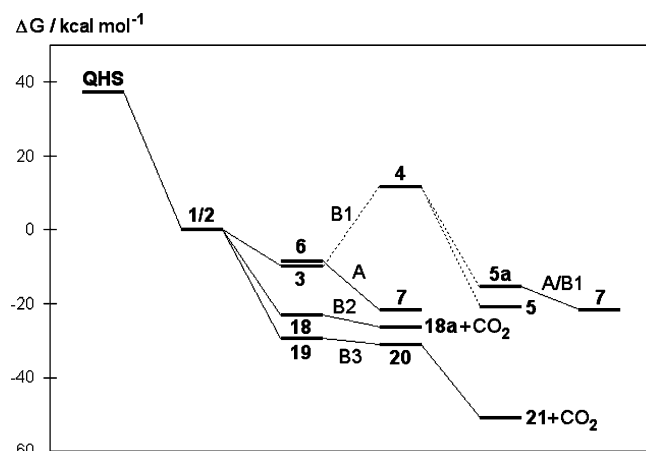


Figure 9. Gibbs free energy diagram corresponding for the four routes of artemisinin reductive decomposition. The uncertain role of **4** is marked by dashed grey lines.

3.3.1. Routes B2 and B3. Route B2 begins with the O-centered radical transformation **2** → **18** which is exothermic. But the next step, formation of the C-centered radical **18a** and CO₂ release, seems to consume energy, so the final formation of **18a**+CO₂ from **2** is slightly exothermic (Tables 5 and 6). This indicates that the unpaired electron delocalization within the carboxyl group stabilizes the radical (Figure 8), so another decomposition mechanism could occur besides the CO₂ release.

However, B3 starts with highly exothermic transformation **2** → **19** (Table 5), resulting in the C-centered radical **19** that is more stable than the O-centered radical **18** by 9.0 kcal mol⁻¹ (Table 4). Oxidation of **19** into **20** is slightly exothermic, but the CO₂ release yields more energy (Table 5). Route B3 is obviously energetically more favorable than B2 by 27.3 kcal mol⁻¹ (Table 6).

3.4. Free Energy Description of the Artemisinin Decomposition (25 °C). Results for free energy and entropy calculations at 25 °C are presented in Tables 4–6 parallel with electronic energies. There is a good agreement between electronic and free energies in Table 4 (correlation coefficient is 0.93), while the total entropy generally increases along the decomposition routes. It is visible that the entropy change is rather high for species involved in CO₂ releases and species with side chains (being greater than 150 cal mol⁻¹ K⁻¹ for **6** and all species in routes B2 and B3), due to the increase in the number of particles and flexible fragments, respectively. Cumulative effects of these entropy trends and of thermal motion contributions to the free energy are visible in Tables 5 and 6 and Figure 9. Entropy changes Δ*S* superior to 20 cal mol⁻¹ K⁻¹ occur for conversions along the B2 and B3 routes, making the free energy differences ΔΔ*G* much more negative than Δ*E*_e for these reactions (Table 5) and the routes (ΔΔ*G* below -60 kcal mol⁻¹, see Table 6). However, **4**, **5**, **5a**, and **7** are not characterized by higher total entropy than the species by which they are preceded (Table 4). This is the reason why conversions including these species (with exception of **5a** → **7**) have negative Δ*S*, and, consequently, more negative Δ*E*_e than ΔΔ*G* (Table 5), and results in small positive Δ*S* values and very similar Δ*E*_e and almost identical ΔΔ*G* for routes A and B1 (Table 6). B2 and B3 are thermodynamically more favorable, especially B3 (ΔΔ*G* = -88 kcal mol⁻¹), but include more decomposi-

tion steps and, thus, kinetically could be less favorable. Accordingly, the literature^{10,11,41,47} reports most decomposition products are from the A and B1 routes which can be interconnected. Activation energies for particular conversions have been reported to range from 4 to 9 kcal mol⁻¹.^{25,26,28} It is noteworthy to mention the high endothermicity of conversion **3** → **4** (ΔΔ*G* = 21.3 kcal mol⁻¹, Table 5), which indicates that **4** does not exist in route A and that removal of Fe(II) causes simultaneous rearrangements of C–O and H–O bonds in **3** yielding **5** or **5a**. **4** was reported by Wu et al.⁴⁴ as a minor product of artemisinin decomposition. It was reported by Taranto et al.³¹ as a very unstable species that did not belong to the main routes of artemisinin decomposition. The molecular structure of **4** (Figure 6), especially the conformation of its seven-membered ring oxacycloheptane, can explain why this intermediate is substantially unstable with respect to **3**, **5**, and **5a** (Figure 9). Formation of the epoxide ring at C3 and C4 causes nearly planar conformation of the fragment O13–C3–C4–C5 with bond angles in the range 122–128°. Such a strained ring, in the absence of iron, causes significant local and global instability of the molecular system. The radical **3** must rearrange into **5** or **5a** via some other mechanism.

3.5. Integral Description of the Artemisinin Decomposition. Oxygen–oxygen 1,3- and 1,4-interactions are characterized by distances 2.2–2.3 Å in **QHS** and rings of other species from Figure 2 and also in the artemisinins structures from the CSD (Table C). Besides all which has already been said about this type of interactions, there are two more reasons to consider related structural descriptors. First, oxygen–oxygen distances of 2.2–2.3 Å can be attributed to considerable energy, as for example during O–O bond dissociation in O₂ (3–9 kcal mol⁻¹ according to some accurate calculations⁸⁷). Second, some studies⁸⁸ on 1,5-interactions between oxygen atoms in organic molecules have shown that these interactions can be classified as closed shell bonding interactions and not repulsions, accounting for at least 10 kcal mol⁻¹ in molecular energy stabilization.

According to these observations, six electronic and structural descriptors were defined and presented in Table 7 for 13 species from Figure 2 (**QHS**, **1/2**, **3**, **4**, **5**, **5a**, **6**, **7**, **18**, **18a**, **19**, **20**, and **21**): *E*_{er} – electronic energy relative to **1/2** (including that of CO₂), Δ*G*_r – Gibbs energy relative to **1/2** (including that of CO₂), *d*(O1–O2) – O1–O2 distance, <*d*(O–O)> – average O–O distance (CO₂ is excluded), lnPLw – natural logarithm of Löwdin bond order for the O1–O2 distance, and <lnPLw> – average of natural logarithms of Löwdin bond orders for the O–O distances. The autoscaled data matrix with dimensions 13 × 6 was analyzed by PCA and HCA (incremental linkage), and the results are presented in Figure 10.

The HCA dendrogram (Figure 10, left) exhibits two distinct clusters: the smaller cluster formed only from species from the B2 and B3 routes (**18**, **18a**, **19**, **20**, and **21**) at similarity index 0.59, and the bigger cluster in which the species from the A and B1 routes (**1/2**, **3**, **4**, **5**, **5a**, **6**, and **7**) are grouped with **QHS** at lower similarity index 0.38. Besides, radicals tend to form subclusters (**18**, **18a** and **19**; **3** and **1/2**) or separate from the rest (**6**).

The PC1 scores plot (Figure 10, right) corresponds to 71.8% of the original data, showing the two clusters as defined in HCA, discriminated by PC1 about the value PC1

Table 7. Six Electronic^a and Structural^b Descriptors of the Artemisinin Decomposition Routes

species	$E_{er}/\text{kcal mol}^{-1}$	$\Delta G_r/\text{kcal mol}^{-1}$	$d(\text{O1}-\text{O2})/\text{\AA}$	$\langle d(\text{O}-\text{O}) \rangle/\text{\AA}$	$\ln\text{PLw}$	$\langle \ln\text{PLw} \rangle$
QHS	33.33	37.25	1.460	3.078	0.1240	-4.3679
1/2	0.00	0.00	2.186	3.211	-1.4619	-4.4146
3	-7.09	-9.73	2.434	3.268	-2.3424	-4.6167
4	8.15	11.55	2.700	3.289	-3.3439	-4.8086
5	-24.29	-20.82	2.806	3.802	-5.1328	-5.1423
5a	-19.65	-15.23	2.713	3.215	-3.9477	-4.6604
7	-22.87	-21.64	2.999	3.133	-5.1850	-4.5148
20	-25.36	-31.15	3.328	4.121	-5.3185	-6.7352
21	-32.61	-51.00	3.328	4.840	-5.3185	-7.8703
6	-0.72	-8.46	4.720	3.518	-5.9915	-4.5479
18	-13.43	-22.97	5.000	5.891	-6.9078	-6.2422
18a	-5.29	-26.32	4.872	4.586	-6.1193	-5.7890
19	-22.40	-29.28	4.812	4.678	-6.5023	-6.0143

^a Electronic descriptors: E_{er} , ΔG_r – electronic energy and free energy relative to **1/2** (including that of CO_2), respectively. ^b Structural descriptors: $d(\text{O1}-\text{O2})$ – distance between peroxide oxygen atoms O1 and O2, $\langle d(\text{O}-\text{O}) \rangle$ – average oxygen–oxygen distance (CO_2 is excluded), $\ln\text{PLw}$ – natural logarithm of Löwdin bond order for the O1–O2 distance, and $\langle \ln\text{PLw} \rangle$ – average of natural logarithms of Löwdin bond orders for the O–O distances.

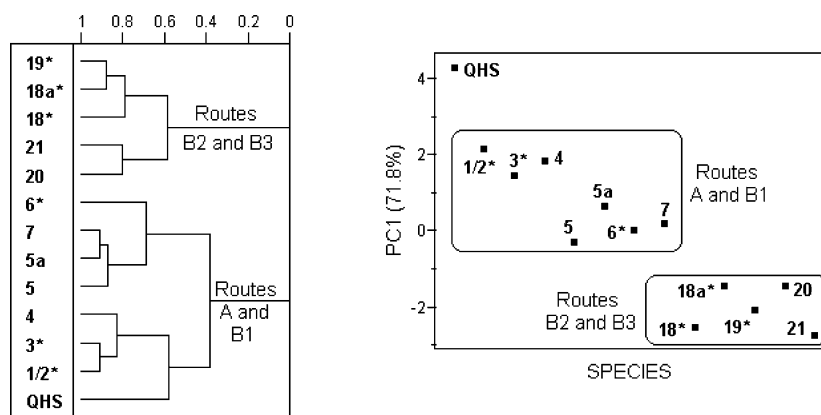


Figure 10. Left: Dendrogram obtained from six electronic and structural descriptors of **QHS** and species from artemisinin decomposition. Right: PC1 scores plot for the same data set. Radicals are marked with an asterisk (*).

= -1. **QHS** could be considered as isolated at maximum PC1 values. However, species of the bigger cluster are structurally more similar to **QHS** than other samples, since routes A and B1 include more ring structures. The smaller cluster is obviously characterized by larger $\langle d(\text{O}-\text{O}) \rangle$ (>4 Å), more negative ΔG_r (<-22 kcal mol⁻¹) and more negative $\langle \ln\text{PLw} \rangle$ (<-5.5) than the bigger cluster. Besides, the species of the small cluster have the bond-per-atom-ratio (including and also excluding H atoms) equal one, while the other species have greater ratios due to more rings in structures. Routes A and B1 are being related via the A/B1 route and start with the same radical **1/2**, while routes B2 and B3 start with the common radical **2** and include structures with only one ring. These properties in common for the route pairs may be responsible for the clustering pattern along PC1.

The artemisinin decomposition routes studied in this work show that larger structural changes, which necessarily result in more branched and flexible structures, lead to more stable species in which interatomic distances and bond orders substantially decrease. Therefore, weakening of oxygen–oxygen nonbonding interactions is a consequence of the **QHS** decomposition, well visible from the correlation of E_{er} and ΔG_r with $d(\text{O1}-\text{O2})$ for species excluding radicals from B2 and B3 (**QHS**, **1/2**, **3**, **4**, **5**, **5a**, **7**, **20**, and **21**): the correlation coefficients are equal to -0.90. These facts make it possible to predict the stability of other decomposition species which were not considered in this work, based on their molecular

structures. Total entropy S_{tot} (Table 4) is an intrinsic property of the species that is well-related to the clustering pattern along PC1: 129 for **QHS**, 130–152 for routes A and B1, and 151–194 cal mol⁻¹ K⁻¹ for routes B2 and B3. S_{tot} is reasonably well correlated with PC1 (correlation coefficient is -0.75) because of correlations with descriptors ΔG_r , $d(\text{O1}-\text{O2})$, $\langle d(\text{O}-\text{O}) \rangle$, $\ln\text{PLw}$, and $\langle \ln\text{PLw} \rangle$ (correlation coefficients are -0.69, 0.63, 0.71, -0.59, and -0.81, respectively). Structural changes along the decomposition routes (Figure 2) confirm that the entropy increase is one of the driving forces of the decomposition. Therefore, disruption of O–O interactions, which are attractive by their nature, is a good indicator of the degree of artemisinin decomposition.

4. CONCLUSIONS

The density functional theory study of the artemisinin reductive decomposition routes A, B1, B2, and B3 included 13 species: **QHS**, **1/2**, **3**, **4**, **5**, **5a**, **6**, **7**, **18**, **18a**, **19**, **20**, and **21**. The study was supported with appropriate structural and chemometric approaches in order to rationalize the relationships between the routes. The A and B1 routes can be interconnected via the A/B1 route. This fact and other common features of the involved species make routes A and B1 mutually similar and rather distinct from routes B2 and B3 which are similar to each other. Such a clustering pattern corresponds to the fact that B2 and B3 are thermodynamically

cally more preferred ($\Delta\Delta G$ is -64 and -88 kcal mol $^{-1}$, respectively) than A and B1 ($\Delta\Delta G$ is -58 and -59 kcal mol $^{-1}$, respectively), but A and B1 may be kinetically favored as the literature confirms. Artemisinin reductive decomposition, especially its routes B2 and B3, shows that larger structural changes, i.e., formation of branched structures and CO $_2$ release are well accompanied by increased exothermicity of the conversions, weakening of attractive oxygen–oxygen interactions, and increased entropy of the formed species and the reactions. It is clear that the intermediate **4** belongs to some alternative and minor artemisinin decomposition route.

ACKNOWLEDGMENT

CENAPAD-SP and FAPESP are gratefully acknowledged for financial support. The authors also acknowledge Dr. Carol H. Collins for English revision.

Supporting Information Available: Figure and two tables for oxygen–oxygen bond length–bond order relationship, a list of CSD codes with references for crystal structures of artemisinins, and a table with selected structural data for these structures with a figure showing important correlations for these data. This material is available free of charge via the Internet at <http://pubs.acs.org>.

REFERENCES AND NOTES

- (1) *The World Health Report 2005: Make every mother and child count*; World Health Organization (WHO) Press: Geneva, 2005; p 44. http://www.who.int/whr/2002/en/whr02005_en.pdf (accessed June 21, 2007).
- (2) Bowman, S.; Lawson, D.; Brown, D.; Chillingworth, T.; Churcher, C. M.; Craig, A.; Davies, R. M.; Devlin, K.; Squares, R.; Squares, S.; Sulston, J. E.; Whitehead, S.; Woodward, J. R.; Newbold, C.; Barrell, B. G. The Complete Nucleotide Sequence of Chromosome 3 of *Plasmodium falciparum*. *Nature* **1999**, *400*, 532–538.
- (3) O'Neill, P. M.; Bray, P. G.; Hawley, S. R.; Ward, S. A.; Park, B. K. 4-Aminoquinolines - Past, Present, and Future: A Chemical Perspective. *Pharmacol. Ther.* **1998**, *77*, 29–58.
- (4) Moore, D. V.; Lanier, J. E. Observations on Two *Plasmodium falciparum* Infections with an Abnormal Response to Chloroquine. *Am. J. Trop. Med. Hyg.* **1961**, *10*, 5–9.
- (5) Mockenhaupt, F. P. Mefloquine Resistance in *Plasmodium falciparum*. *Parasitol. Today* **1995**, *11*, 248–254.
- (6) Klayman, D. L. Qinghaosu (Artemisinin): an Antimalarial Drug from China. *Science* **1985**, *228*, 1049–1055.
- (7) Fidock, D. A.; Rosenthal, P. J.; Croft, S. L.; Brun, R.; Nwaka, S. Antimalarial drug discovery: efficacy models for compound screening. *Nat. Rev.* **2004**, *3*, 509–520.
- (8) Haynes, R. K.; Ho, W.-Y.; Chan, H.-W.; Fugmann, B.; Stetter, J.; Croft, S. L.; Vivas, L.; Peters, W.; Robinson, B. L. Highly Antimalarial-Active Artemisinin Derivatives: Biological Activity Does Not Correlate with Chemical Reactivity. *Angew. Chem., Int. Ed. Engl.* **2004**, *43*, 1381–1385.
- (9) Krungkrai, S. R.; Yuthavong, Y. The Antimalarial Action on *Plasmodium falciparum* of Qinghaosu and Artesunate in Combination with Agents which Modulate Oxidant Stress. *Trans. R. Soc. Trop. Med. Hyg.* **1987**, *81*, 710–714.
- (10) Jefford, C. W.; Vicente, M. G. H.; Jacquier, Y.; Favarger, F.; Mareda, J.; Millasson-Schmidt, P.; Brunner, G.; Burger, U. The Deoxygenation and Isomerization of Artemisinin and Artemether and Their Relevance to Antimalarial Action. *Helv. Chim. Acta* **1996**, *79*, 1475–1487.
- (11) Cumming, J. N.; Ploypradith, P.; Posner, G. H. Antimalarial Activity of Artemisinin (Qinghaosu) and Related Trioxanes: Mechanism(s) of Action. *Adv. Pharmacol.* **1997**, *37*, 253–297.
- (12) Meshnik, S. R.; Taylor, T. E.; Kamchonwongpaisan, S. Artemisinin and the Antimalarial Endoperoxides: from Herbal Remedy to Targeted Chemotherapy. *Microbiol. Rev.* **1996**, *60*, 301–315.
- (13) Francis, S. E.; Sullivan, D. J.; Goldberg, D. E. Hemoglobin Metabolism in the Malaria Parasite *Plasmodium falciparum*. *Ann. Rev. Microbiol.* **1997**, *51*, 97–123.
- (14) Slater, A. F. G. Chloroquine Mechanism of Drug Action and Resistance in *Plasmodium falciparum*. *Pharmacol. Ther.* **1993**, *57*, 203–235.
- (15) Boucher, I. A.; Brzozowski, A. M.; Brannigan, J. A.; Schnick, C.; Smith, D. J.; Kyes, S. A.; Wilkinson, A. I. The crystal structure of superoxide dismutase from *Plasmodium falciparum*. *BMC Struct. Biol.* **2006**, *6*, 20. <http://www.biomedcentral.com/1472-6807/6/20/> (accessed June 19, 2007).
- (16) Kimata-Aruga, Y.; Kurisu, G.; Hase, T. Redox power generator of a nonphotosynthetic plastid in malaria parasite. The data deposited at the Protein Data Bank, PDB ID: 1IUUE. <http://www.rcsb.org/pdb/explore.do?structureId=1IUUE> (accessed June 16, 2007).
- (17) Robert, A.; Cazelles, J.; Meunier, B. Characterization of the Alkylation Product of Heme by the Antimalarial Drug Artemisinin. *Angew. Chem., Int. Ed. Engl.* **2001**, *40*, 1954–1957.
- (18) Cazelles, J.; Robert, A.; Meunier, B. Alkylating Capacity and Reaction Products of Antimalarial Trioxanes after Activation by a Heme Model. *J. Org. Chem.* **2002**, *67*, 609–619.
- (19) Posner, G. H.; Oh, C. H.; Wang, D.; Gerena, L.; Milhous, W. K.; Meshnik, S. R.; Asawamahasadka, W. Mechanism-Based Design, Synthesis, and in Vitro Antimalarial Testing of New 4-Methylated Trioxanes Structurally Related to Artemisinin: The Importance of a Carbon-Centered Radical for Antimalarial Activity. *J. Med. Chem.* **1994**, *37*, 1256–1258.
- (20) Posner, G. H.; Oh, C. H. A Regiospecifically Oxygen-18 Labeled 1,2,4-Trioxane: A Simple Chemical Model System to Probe the Mechanism(s) for the Antimalarial Activity of Artemisinin (Qinghaosu). *J. Am. Chem. Soc.* **1992**, *114*, 8328–8329.
- (21) Posner, G. H.; Park, S. B.; González, L.; Wang, D.; Cumming, J. N.; Klinedinst, D.; Shapiro, T. A.; Bachi, M. D. Evidence for the Importance of High-Valent Fe=O and of a Diketone in the Molecular Mechanism of Action of Antimalarial Trioxane Analogs of Artemisinin. *J. Am. Chem. Soc.* **1996**, *118*, 3537–3538.
- (22) Eckstein-Ludwig, U.; Webb, R. J.; van Goethem, I. D. A.; East, J. M.; Lee, A. G.; Kimura, M.; O'Neill, P. M.; Bray, P. G.; Ward, S. A.; Krishna, S. Artemisinins Target the SERCA of *Plasmodium falciparum*. *Nature* **2003**, *424*, 957–961.
- (23) Haynes, R. K.; Monti, D.; Taramelli, D.; Basilico, N.; Parapini, S.; Oliario, P. Artemisinin Antimalarials Do Not Inhibit Hemozoin Formation. *Antimicrob. Agents Chemother.* **2003**, *47*, 1175.
- (24) Gu, J. D.; Chen, K. X.; Jiang, H. L.; Leszczynski, J. A Model Molecule Study of the O-Centered and the C-Centered Free Radical Intermediates of Artemisinin. *J. Mol. Struct. (THEOCHEM)* **1999**, *491*, 57–66.
- (25) Gu, J.; Chen, K.; Jiang, H.; Leszczynski, J. The Radical Transformation in Artemisinin: A DFT Study. *J. Phys. Chem. A* **1999**, *103*, 9364–9369.
- (26) Tonmuphean, S.; Parasuk, V.; Kokpol, S. Effective Discrimination of Antimalarial Potency of Artemisinin Compounds Based on Quantum Chemical Calculations of their Reaction Mechanism. *Bioorg. Med. Chem.* **2006**, *14*, 2082–2088.
- (27) Rafiee, M. A.; Hadipour, N. L.; Naderi-manesh, H. The Role of Charge Distribution on the Antimalarial Activity of Artemisinin Analogues. *J. Chem. Inf. Model.* **2005**, *45*, 366–370.
- (28) Tonmuphean, S.; Parasuk, V.; Kokpol, S. Theoretical Investigations on Reaction Mechanisms of Artemisinin Compounds: Effect of Structure on Kinetic Energy Profile and Antimalarial Activity. *J. Mol. Struct. (THEOCHEM)* **2005**, *724*, 99–105.
- (29) Moles, P.; Oliva, M.; Safont, V. S. Modeling the Decomposition Mechanism of Artemisinin. *J. Phys. Chem. A* **2006**, *110*, 7144–7158.
- (30) Drew, M. G. B.; Metcalfe, J.; Ismail, F. M. D. Antimalarial drugs based on artemisinin: DFT calculations on the principal reactions. *J. Mol. Struct. (THEOCHEM)* **2005**, *756*, 87–95.
- (31) Taranto, A. G.; Carneiro, J. W. M.; Araújo, M. T. DFT Study of the Reductive Decomposition of Artemisinin. *Bioorg. Med. Chem.* **2006**, *14*, 1546–1557.
- (32) Drew, M. G. B.; Metcalfe, J.; Dascombe, M. J.; Ismail, F. M. D. Reactions of Artemisinin and Artheether with Acid: Implications for Stability and Mode of Antimalarial Action. *J. Med. Chem.* **2006**, *49*, 6065–6073.
- (33) Galasso, V.; Kovač, B.; Modelli, A. A theoretical and experimental study on the molecular and electronic structures of artemisinin and related drug molecules. *Chem. Phys.* **2007**, *335*, 141–154.
- (34) Tonmuphean, S.; Parasuk, V.; Kokpol, S. Automated Calculation of Docking of Artemisinin to Heme. *J. Mol. Model.* **2001**, *7*, 26–33.
- (35) Pinheiro, J. C.; Kiralj, R.; Ferreira, M. M. C. Artemisinin Derivatives with Antimalarial Activity against *Plasmodium falciparum* Designed with the aid of Quantum Chemical and Partial Least Squares Methods. *QSAR Comb. Sci.* **2003**, *22*, 830–842.
- (36) Pinheiro, J. C.; Ferreira, M. M. C.; Romero, O. A. S. Antimalarial activity of dihydroartemisinin derivatives against *P. falciparum* resistant to mefloquine: a quantum chemical and multivariate study. *J. Mol. Struct. (THEOCHEM)* **2001**, *572*, 35–44.
- (37) Avery, M. A.; Alvim-Gaston, M.; Rodrigues, C. R.; Barreiro, E. J.; Cohen, F. E.; Sabnis, Y. A.; Woolfrey, J. R. Structure-Activity Relationships of the Antimalarial Agent Artemisinin. 6. The Develop-

- ment of Predictive In Vitro Potency Models Using CoMFA and HQSAR Methodologies. *J. Med. Chem.* **2002**, *45*, 292–303.
- (38) Silva, M. C.; Kiralj, R.; Ferreira, M. M. C. Estudo Teórico da Interação Existente Entre a Artemisinina e Heme. *Quim. Nova* **2006**, *30*, 25–31.
- (39) Tonmunphean, S.; Parasuk, V.; Kokpol, S. QSAR Study of Antimalarial Activity and Artemisinin-Heme Binding Properties Obtained from Docking Calculations. *Quant. Struct.-Act. Relat.* **2000**, *19*, 475–483.
- (40) Denisov, E.; Denisova, T.; Ismail, F. Intramolecular Reactions of Free Radicals Formed from Artemisinin. *Int. J. Chem. Kinet.* **2005**, *37*, 554–565.
- (41) Wu, Y.; Liu, H.-H. Cleavage of Qinghaosu (Artemisinin) Induced by Non-Iron Transition-Metal Ions in the Presence of Excess Cysteine. *Helv. Chim. Acta* **2003**, *86*, 3074–3080.
- (42) Creek, D. J.; Chiu, F. C. K.; Prankerd, R. J.; Charman, S. A.; Charman, W. N. Kinetics of Iron-Mediated Artemisinin Degradation: Effect of Solvent Composition and Iron Salt. *J. Pharm. Sci.* **2005**, *94*, 1820–1829.
- (43) Wu, W.-M.; Wu, Y.-L. Chemical and electro-chemical reduction of qinghaosu (artemisinin). *J. Chem. Soc., Perkin Trans. 1* **2000**, 4279–4283.
- (44) Wu, W.-M.; Wu, Y.; Wu, Y.-L.; Yao, Z.-J.; Zhou, C.-M.; Li, Y.; Shan, F. Unified Mechanistic Framework for the Fe(II)-Induced Cleavage of Qinghaosu and Derivatives/Analogues. The First Spin-Trapping Evidence for the Previously Postulated Secondary C-4 Radical. *J. Am. Chem. Soc.* **1998**, *120*, 3316–3325.
- (45) Mei-Yi, Z.; Lan-Na, L.; Shu-Feng, C.; Guang-Yi, L.; Xiao-Tian, L.; Chen, M.; Clardy, J. Chemical transformation of qinghaosu, a peroxidic antimalarial. *Tetrahedron* **1983**, *39*, 2941–2946.
- (46) Kapetanaki, S.; Varotsis, C. Fourier Transform Infrared Investigation of Non-Heme Fe(III) and Fe(II) Decomposition of Artemisinin and of a Simplified Trioxane Alcohol. *J. Med. Chem.* **2001**, *44*, 3150–3156.
- (47) Lin, A. J.; Klayman, D. L.; Hoch, J. M.; Silverton, J. V.; George, C. F. Thermal Rearrangement and Decomposition Products of Artemisinin (Qinghaosu). *J. Org. Chem.* **1985**, *50*, 4504–4508.
- (48) Madhusudana, K. P.; Vishwakarma, R. A.; Balachandran, S.; Popli, S. P. Mass spectral studies on artemisinin, dihydroartemisinin and artemether. *Ind. J. Chem. B* **1989**, *28*, 751–754.
- (49) Chen, H.-H.; Zhou, H.-J.; Fang, X. Inhibition of human cancer cell line growth and human umbilical vein endothelial angiogenesis by artemisinin derivatives in vitro. *Pharm. Res.* **2003**, *48*, 231–236.
- (50) Wartenberg, M.; Wolf, S.; Budde, P.; Grünheck, F.; Acker, H.; Hescheler, J.; Wartenberg, G.; Sauer, H. The Antimalarial Agent Artemisinin Exerts Antiangiogenic Effects in Mouse Embryonic Stem Cell-Derived Embryoid Bodies. *Lab. Invest.* **2003**, *83*, 1647–1655.
- (51) Bhattacharjee, A. K.; Karle, J. M. Stereoelectronic Properties of Antimalarial Artemisinin Analogues in Relation to Neurotoxicity. *Chem. Res. Toxicol.* **1999**, *12*, 422–428.
- (52) Novak, I.; Kovač, B. Photoelectron Spectra of Important Drug Molecules: Zidovudine and Artemisinin. *J. Org. Chem.* **2003**, *68*, 5777–5779.
- (53) Frisch, M. J.; Trucks, G. W.; Schlegel, H. B.; Scuseria, G. E.; Robb, M. A.; Cheeseman, J. R.; Zakrzewski, V. G.; Montgomery, J. A.; Stratmann, R. E.; Burant, J. C.; Dapprich, S.; Millam, J. M.; Daniels, A. D.; Kudin, K. N.; Strain, M. C.; Farkas, O.; Tomasi, J.; Barone, V.; Cossi, M.; Cammi, R.; Mennucci, B.; Pomelli, C.; Adamo, C.; Clifford, S.; Ochterski, J.; Petersson, G. A.; Ayala, P. Y.; Cui, Q.; Morokuma, K.; Malick, D. K.; Rabuck, A. D.; Raghavachari, K.; Foresman, J. B.; Cioslowski, J.; Ortiz, J. V.; Stefanov, B. B.; Liu, G.; Liashenko, A.; Piskorz, P.; Komaromi, I.; Gomperts, R.; Martin, R. L.; Fox, D. J.; Keith, T.; Al-Laham, M. A.; Peng, C. Y.; Nanayakkara, A.; Gonzalez, C.; Challacombe, M.; Gill, P. M. W.; Johnson, B. G.; Chen, W.; Wong, M. W.; Andres, J. L.; Head-Gordon, M.; Replogle, E. S.; Pople, J. A. *Gaussian 98W, version 5.4, Revision A.1*; Gaussian, Inc.: Pittsburgh, PA, 1998.
- (54) *Titan, version 1.0.8*; Wavefunction, Inc.: Schrodinger, Portland, OR, Wavefunction, Inc.: Irvine, CA, 2001.
- (55) Becke, A. D. Density-Functional Thermochemistry. 3. The Role of Exact Exchange. *J. Chem. Phys.* **1993**, *98*, 5648–5652.
- (56) Lee, C. T.; Yang, W. T.; Parr, R. G. Development of the Colle-Salvetti Correlation-Energy Formula Into A Functional Of The Electron Density. *Phys. Rev. B* **1988**, *37*, 785–789.
- (57) Allen, F. H. The Cambridge Structural Database: a quarter of a million crystal structures and rising. *Acta Crystallogr., Sect. B: Struct. Sci.* **2002**, *58*, 380–388.
- (58) *Cambridge Structural Database, version 5.28 with the January and May 2007 Updates*; Cambridge Structural Data Centre, University of Cambridge: Cambridge, U.K., November 2006.
- (59) Bruno, I. J.; Cole, J. C.; Edgington, P. R.; Kessler, M.; Macrae, C. F.; McCabe, P.; Pearson, J.; Taylor, R. New software for searching the Cambridge Structural Database and visualizing crystal structures. *Acta Crystallogr., Sect. B: Struct. Sci.* **2002**, *58*, 389–397.
- (60) *ConQuest, version 1.9*; Cambridge Structural Data Centre, University of Cambridge: Cambridge, U.K., 2006.
- (61) *Vista, version 2.1c*; Cambridge Structural Data Centre, University of Cambridge: Cambridge, U.K., 2006.
- (62) Lisgarten, J. N.; Potter, B. S.; Bantuzeko, C.; Palmer, R. A. Structure, Absolute Configuration, and Conformation of the Antimalarial Compound, Artemisinin. *J. Chem. Cryst.* **1998**, *28*, 539–543.
- (63) Beebe, K. R.; Pell, R. J.; Seasholtz, M. B. *Chemometrics: A Practical Guide*; John Wiley & Sons: New York, 1998.
- (64) Wold, S.; Esbensen, K.; Geladi, P. Principal Component Analysis. *Chemom. Intell. Lab. Syst.* **1987**, *2*, 37–52.
- (65) *Pirouette, version 3.01*; Infometrix, Inc.: Woodinville, WA, 2001.
- (66) Leban, I.; Golič, L.; Japelj, M. Crystal And Molecular Structure of Qinghaosu – A Redetermination. *Acta Pharm. Jugosl.* **1988**, *38*, 71–77.
- (67) Jefford, C. W.; Burger, U.; Millasson-Schmidt, P.; Bernardinelli, G.; Robinson, B. L.; Peters, W. Epiartemisinin, a Remarkably Poor Antimalarial: Implications for the Mode of Action. *Helv. Chim. Acta* **2000**, *83*, 1234–1246.
- (68) Taranto, A. G.; Carneiro, J. W. M.; Oliveira, F. G.; Araújo, M. T.; Correa, C. R. The Role of C-Centered Radicals on the Mechanism of Action of Artemisinin. *J. Mol. Struct. (THEOCHEM)* **2002**, *580*, 207–215.
- (69) Lewiński, J.; Zachara, J.; Justyniak, I. Directionality and borderline distance of secondary bonding on the fifth coordinate site in aluminium alkoxides. *Chem. Commun.* **2002**, 1586–1587.
- (70) Eckert-Maksić, M.; Novak-Doumbouya, N.; Kiralj, R.; Kojić-Prodić, B. 7-Oxanorborene cycloadducts. X-Ray, molecular orbital and photoelectron spectroscopic study. *J. Chem. Soc., Perkin Trans 2* **2000**, 1483–1487.
- (71) Löwdin, P. O. On the Non-Orthogonality Problem. *Adv. Quantum Chem.* **1970**, *5*, 185–199.
- (72) Gu, J.; Chen, K.; Jiang, H.; Chen, J. Z.; Ji, R. A DFT Study of Artemisinin and 1,2,4-Trioxane. *J. Mol. Struct. (THEOCHEM)* **1999**, *459*, 103–111.
- (73) Gu, J.; Chen, K.; Jiang, H.; Zhu, W. L.; Chen, J. Z.; Ji, R. A Quantum Chemistry Study of Qinghaosu. *Chem. Phys. Lett.* **1997**, *277*, 234–238.
- (74) *CRC Handbook of Chemistry and Physics*, 87th ed. (2006–2007 ed.); Lide, D., Ed.; CRC Press: Boca Raton, FL, 2006; Section 9, pp 9–22.
- (75) Bridgeman, A. J.; Rothery, J. Bonding in mixed halogen and hydrogen peroxides. *J. Chem. Soc., Dalton Trans.* **1999**, 4077–4082.
- (76) Tonmunphean, S.; Irle, S.; Kokpol, S.; Parasuk, V.; Wolschann, P. Ab initio and density functional study on singlet and triplet states of artemisinin. *J. Mol. Struct. (THEOCHEM)* **1998**, *454*, 87–90.
- (77) *International Tables for Crystallography, Vol. C: Mathematical, Physical and Chemical Tables*, 3rd ed.; Prince, E., Ed.; International Union of Crystallography by Kluwer Academic Publishers: Dordrecht, The Netherlands, 2004; p 789.
- (78) Farrugia, L. J. *Platon for Windows Taskbar, v. 1.10*; University of Glasgow: Glasgow, U.K., 2006.
- (79) Tang, Y.; Dong, Y.; Wang, X.; Sriraghavan, K.; Wood, J. K.; Vennerstrom, J. L. Dispiro-1,2,4-trioxane Analogues of a Prototype Dispiro-1,2,4-trioxolane: Mechanistic Comparators for Artemisinin in the Context of Reaction Pathways with Iron(II). *J. Org. Chem.* **2005**, *70*, 5103–5110.
- (80) Bloodworth, A. J.; Shah, A. Iron(II)-mediated Rearrangement of 1,2,4-Trioxanes into 1,2-Diol Monoesters via 1,5-Hydrogen Transfer. *Tetrahedron Lett.* **1995**, *36*, 7551–7554.
- (81) Avery, M. A.; Fan, P.; Karle, J. M.; Bonk, J. D.; Miller, R.; Goins, D. K. Structure-Activity Relationships of the Antimalarial Agent Artemisinin. 3. Total Synthesis of (+)-13-Carbaartemisinin and Related Tetra- and Tricyclic Structures. *J. Med. Chem.* **1996**, *39*, 1885–1897.
- (82) Luo, X.-D.; Yeh, H. J. C.; Bossi, A.; Flippen-Anderson, J. L.; Gilardi, R. The Chemistry of Drugs. 6. Thermal Decomposition of Qinghaosu. *Heterocycles* **1985**, *23*, 881–887.
- (83) Cafferata, L. F. R.; Jeandupeux, R.; Romanelli, G. P.; Mateo, C. M.; Jefford, C. W. A kinetic and mechanistic study on the thermal decomposition reactions of *cis*-fused 1,2,4-trioxanes and *trans*-fused 1,2,4-trioxanes. *Afinidad* **2003**, *60*, 206–211.
- (84) Cafferata, L. F. R.; Rimada, R. S. Solvent and Substituent Effects on the Thermolysis of Antimalarial Fluorophenyl Substituted 1,2,4-Trioxanes. *Molecules* **2003**, *8*, 655–662.
- (85) Tumanov, V. E.; Denisov, E. T.; Estimation of Enthalpies of Alkoxy Radical Formation and Bond Strengths in Alcohols and Ether. *Kinet. Catal.* **2004**, *45*, 621–627.

- (86) Agapito, F.; Cabral, B. J. C.; Simões, J. A. M. Oxygen-oxygen bond dissociation enthalpies of di-*tert*-butyl peroxide and di-trifluoromethyl peroxide. *J. Mol. Struct. (THEOCHEM)* **2005**, 729, 223–227.
- (87) Su, P.; Song, L.; Wu, W.; Hiberty, P. C.; Shaik, S. A Valence Bond Study of the Dioxygen Molecule. *J. Comput. Chem.* **2007**, 28, 185–197.
- (88) Zhurova, E. A.; Tsirelson, V. G.; Stash, A. I.; Pinkerton, A. A. Characterizing the Oxygen-Oxygen Interaction in the Dinitramide Anion. *J. Am. Chem. Soc.* **2002**, 124, 4574–4575.

CI700011F